High resolution ECG and MCG mapping: simulation study of single and dual accessory pathways and influence of lead displacement and limited lead selection on localisation results

V. JAZBINSEK,* R. HREN, and Z. TRONTELJ

Institute of Mathematics, Physics and Mechanics, University of Ljubljana, 19 Jadranska Str., SI-1000 Ljubljana, Slovenia

Abstract. In this simulation study, we used an anatomical computer model of the human ventricles to simulate body surface potentials and magnetic field for 10 single preexcitation sites and 8 pairs of preexcitation sites positioned on the epicardial surface along the atrio-ventricular ring. We demonstrated that electrocardiographic and magnetocardiographic inverse solutions using a pair of equivalent dipoles could be employed in localising dual accessory pathways. Average localisation errors were in the range of 5 to 21 mm and 3 mm to 20 mm, respectively, when body surface potentials and magnetic field were used. Additionally, we have investigated the influence of random lead displacements and limited lead selection on localisation results.

Key words: electrocardiography, magnetocardiography, accessory pathways, inverse solution.

1. Introduction

Radiofrequency (RF) catheter ablation has become a method of choice in curative treatment of accessory atrioventricular connection in patients suffering from Wolff-Parkinson-White (WPW) syndrome [1]. Prerequisite for the successful ablative treatment is the precise identification of an abnormal pathway. Body-surface potential maps (BSPMs) and magnetic field maps (MFMs) can be reconstructed from noninvasive procedures that involve recording of multiple electrocardiograms and multiple magnetocardiograms, respectively. BSPMs and MFMs have been used to localise preexcitation sites in WPW patients [2,3], where such localisation is performed by calculating the position of an equivalent single dipole source in the model of a human torso.

However, the single-dipole equivalent generator is an adequate approximation only when the bioelectric activity of the heart is confined to a single very small volume. Thus, in cases where more than one preexcitation site is present, more complex equivalent generators (including two or more equivalent dipoles) would achieve better accuracy, and, therefore, a better understanding of the underlying cardiac process. In Section 2 we employ an anatomical computer model to test the hypothesis that dual preexcitation sites can be localised using BSPMs and MFMs in combination with the mathematical inverse solution that uses two single dipoles as an equivalent generator [4].

Although recent advances in development of imaging modalities has made possible to construct patient-specific geometry data, the accurate rendering of electrode positions (leads) on the torso surface is during actual recordings time consuming, labour intensive and often difficult to achieve. To facilitate clinical applications of the single dipole inverse solution, locations of recording leads are approximated using standardised arrays of nodes of individualised torso models. However, such standardised placements of leads are associated with modelling errors. In Section 3 we use computer simulations to quantitatively assess how the localisation accuracy may vary (i) with the random displacement of leads on the torso surface, (ii) with the time after the onset of preexcitation, (iii) with the measurement noise level, and (iv) with location of a given preexcitation site along the atrio-ventricular (A-V) ring [5].

In multichannel recordings of both electrocardiographic and magnetocardiographic signals we typically encounter the problem of redundancy and uniqueness of signal information contained in a large number of leads. To solve this problem, Lux et al. [6] in their seminal work developed a practical method of reducing electrocardiographic leads and applied it to the design of the 32-lead system. This widely-used and convenient system for recording body surface potential maps (BSPMs) has proven its clinical value in detecting spatially limited inhomogeneities of ventricular depolarisation and repolarisation properties (see [7,8] and references therein). In Section 4 we apply the technique developed by Lux [6] to select a limited array of MFM and BSPM recording sites and to study influence of limited lead selection on the source localisation. The choice of the computer simulations as the methodology in this study is supported by their ability to explore capabilities of the inverse solution systematically and under controlled conditions.

2. Dual accessory pathways

2.1. Methods. We used an anatomical model of the human ventricles and a homogeneous model of the human torso to simulate activation at 10 single pacing sites located along right lateral (RL), left lateral (LL), and right/left anteroparaseptal

---

*e-mail: vojko.jazbinsek@imfm.uni-lj.si

V. Jazbinsek, R. Hren, and Z. Trontelj

Table 1
Anatomical description of dual preexcitation sites, see Fig. 1

	Abbreviation	Anatomical Description	Distance*
1a–1b	RAL	right anterolateral	18 mm
1a–1c	RAL/RL	right anterolateral/right lateral	34 mm
1a–1d	RAL/RPL	right anterolateral/right posterolateral	48 mm
2a–2b	LPL/LL	left posterolateral/left lateral	11 mm
2a–2c	LPL/LL	left posterolateral/left lateral	23 mm
2a–2d	LPL/LAL	left posterolateral/left anterolateral	36 mm
3a–3b	RAP/LAP	Right anteroparaseptal/left anteroparaseptal	30 mm
1b–2b	RAL/LPL	right anterolateral/left posterolateral	139 mm

*Distance measured along the AV ring

(RAP/LAP) aspects of the atrio-ventricular (AV) ring of the epicardium (see Fig. 1 and Table 1). This model was developed at Dalhousie University and has been presented in detail in several publications [9–11]. Here, we just briefly summarise the main features of the model. Firstly, the model incorporates an anatomically accurate geometry, with resolution of 0.5 mm. Secondly, it includes the realistic intramural fibre structure with rotating anisotropy. Thirdly, it includes propagation algorithm based on physiological principle of excitatory current flow. The electrotonic interactions of cells are simulated by solving a non-linear parabolic partial differential equation derived from bidomain model. The model behaves as a cellular automata when transmembrane potential exceeds the threshold value. In our earlier validation study [10], we have shown that the morphological features of simulated BSPM patterns (in particular, the position of extrema and the near-zero electric potentials) correspond well with those measured in WPW patients.

For each activation sequence, we simulated corresponding 117-lead BSPMs (covering the anterior and posterior torso), 64-lead MFMs (above the anterior torso) and 128-lead MFMs,
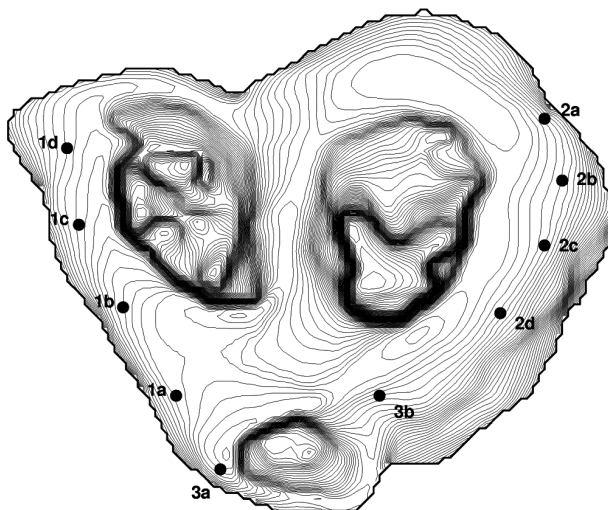

Fig. 1. Basal view of the human ventricular model shown with 10 preexcitation sites. Layers are 1 mm apart, and each is represented by smoothed contour lines to achieve better rendering of the shape. This display illustrates the amount of detail included in the reconstruction of the human ventricular model. Right ventricle is to the left, left ventricle is to the right, and pulmonary artery is to the bottom

see Fig. 2. We positioned an anatomical model of the human myocardium in the homogeneous torso model at heart's anatomical location. Next, we simulated activation sequences with the ventricular model. From this activation sequences, we calculate extracardiac electric potentials and magnetic field with the oblique dipole model of cardiac sources in combination with the boundary element torso model. The infinite medium electric potentials Φ_∞ and magnetic field $\mathbf{B}_\infty$ were determined from the discrete form of equations,

$$
\begin{aligned}
-4\pi\sigma_0\Phi_\infty &= \sigma_1 \int \nabla v_m \cdot \mathbf{r}/r^3 dV \\
&+ \sigma_2 \int \mathbf{a}\mathbf{a}^T \nabla v_m \cdot \mathbf{r}/r^3 dV, \\
-4\pi\sigma_0\mathbf{B}_\infty &= \sigma_1 \int \nabla v_m \times \mathbf{r}/r^3 dV \\
&+ \sigma_2 \int \mathbf{a}\mathbf{a}^T \nabla v_m \times \mathbf{r}/r^3 dV,
\end{aligned}
\tag{1}
$$

where the integrals were evaluated over the ventricular volume, v_m was the transmembrane potential calculated using propagation algorithm, σ_0 was the conductivity of the homogeneous monodomain, σ_1 and σ_2 were conductivities characterising anisotropic myocardium, $\mathbf{a}$ is the local direction of the fibre axis, and $\mathbf{r}$ is the distance from the source point (each activated cell) to a field point. To compute the body surface potentials and magnetic field in the torso model, we used a "fast forward solution" [3,12].

We initiated activation sequences BSPMs and MFMs at 4-ms increments within the first 40 ms after the activation onset. Next, we simulated the sequences initiated at 8 different pairs of sites in the same segments of the AV ring (Fig. 1 and Table 1). To simulate measuring conditions, Gaussian noise at the root-mean-square (RMS) levels of 2.5 μV, 5 μV and 20 μV was added to all simulated BSPMs, and 30 fT, 120 fT and 300 fT was added to all simulated MFMs. We generated 10 different noise distributions for each noise level. Using simulated BSPMs and MFMs as the input data, we performed the inverse solution for a pair of dipole sources in the torso model.

For determining the best initial estimates, we calculated dipole moments from several randomly selected starting dipole positions around the AV ring. The final solution was then obtained with Levenberg-Marquardt least-squares fitting algorithm [5,9]. As a measure of accuracy of the localisation, we used localisation errors, defined as distances between locations

High resolution ECG and MCG mapping: simulation study of single and dual accessory pathways ...
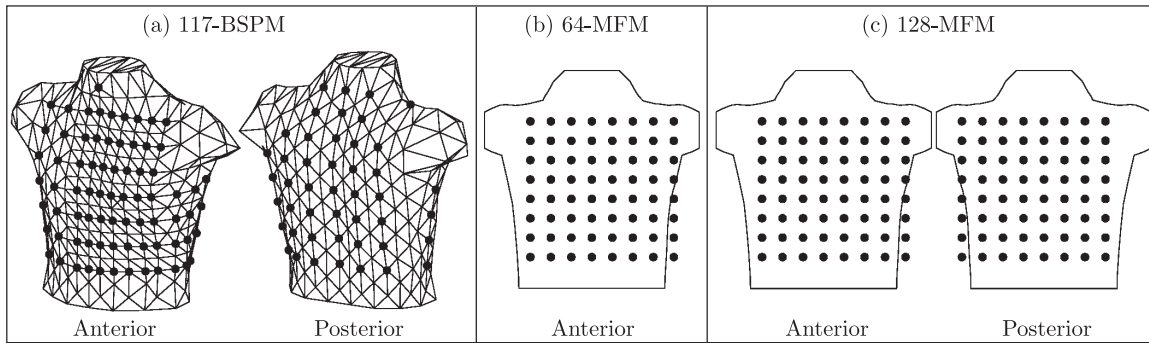

Fig. 2. Schematic layout of a) 117-BSPM, b) 64-MFM and c) 128-MFM leads. The outer boundary of the torso was tessellated with 700 triangles (352 nodes)
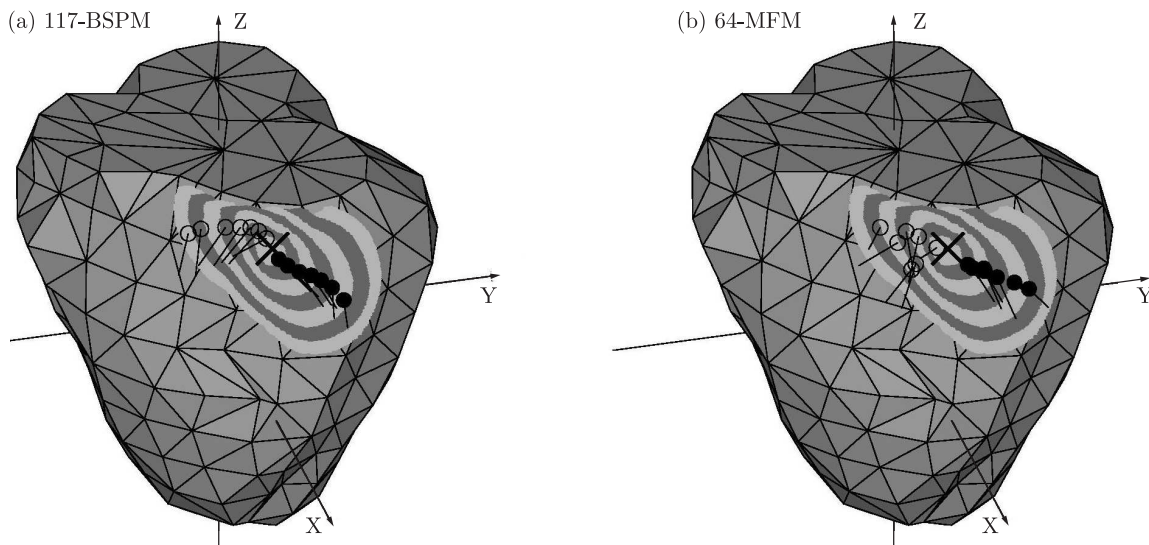

Fig. 3. Localisation of a left-lateral single accessory pathway when using a two-dipole model. Positions of two dipoles reconstructed from 4 to 28 ms after the onset of activation are shown along with the epicardial surface. Inversely-calculated pairs of dipoles when using a) 117-BSPMs and b) 64-MFMs. Inverse solutions were performed under no-noise conditions. The onset of accessory pathway is marked by $\times$; reconstructed positions are labelled as "bullet" and "circle" for the first and the second dipole, respectively, where short lines indicate directions of reconstructed dipole moments. To better illustrate the corresponding activation sequence, alternating light and dark grey zones represent projection of the activation isochronal surface on the epicardial surface between 4 and 28 ms after the onset of activation

of the best-fitting pair of dipoles and a pair of preexcitation sites in the ventricular model. We rejected all solutions for which the magnitude of the stronger of the two dipoles exceeded the weaker dipole by the factor of 5. To account for the influence of the torso's outer boundary on electric potentials, we used an individualised male torso model [10] in simulating BSPMs and MFMs as generated by the ventricular model.

Two-dipole inverse solutions were carried out using the "standard" male torso model. For all inverse solutions, positions of reconstructed dipoles were superimposed on a realistic three-dimensional epicardial surface (that completely encloses the ventricular model) for visual inspection.

2.2. Results. Macchi et al. [13] and Taccardi et al. [14] pointed out that electric potentials during the initial phase of activation resemble those of two opposing dipoles oriented along the major axis and located near the ends of an ellipti-

cal wavefront of propagated activation. To test this hypothesis, we first assessed the performance of a two-dipole generator in localising single accessory pathways. Figure 3 shows a typical example for localisation of a single accessory pathway when using the two-dipole model under ideal (i.e., noise-free) conditions. Localisation of a pair of dipoles is shown at different time instants for an activation sequence initiated at the LL site (2c) when using BSPMs and MFMs. Both reconstructed dipoles are initially in the sequence located close to the site of an accessory pathway, but later become separated by the distance that is progressively increasing with time. The distance between the leading edge of the simulated wavefront and locations of the two corresponding reconstructed dipoles is during the first 28 ms of an activation sequence on average 3 mm (range 1–5 mm). This observation strongly supports the notion that progressive separation of the two dipoles reflects the propagation of an activation wavefront.
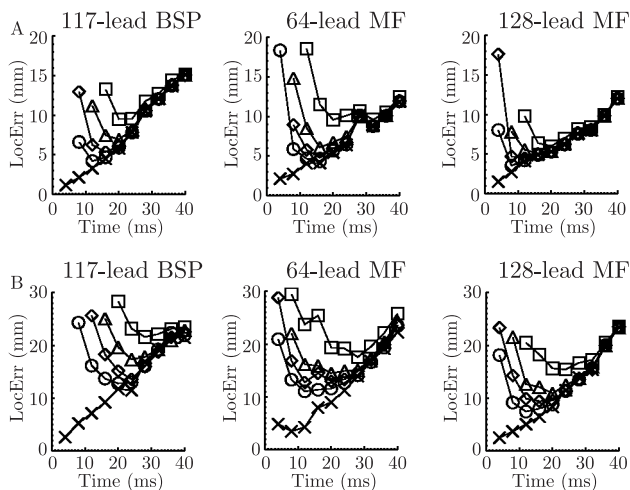
V. Jazbinsek, R. Hren, and Z. Trontelj

Fig. 4. Accuracy of localising a single accessory pathway in the presence of different noise levels when using 117-lead body surface potentials (BSP; "cross" – no noise, "circle" – RMS noise level of 2.5 μV, "diamond" – 5 μV, "triangle" – 10 μV, and "square" – 20 μV), and 64-lead and 128-lead magnetic field (MF-64 and MF-128; "cross" – no noise, "circle" – noise 30 fT, "diamond" – 60 fT, "triangle" – 120 fT, and "square" – 300 fT). Panel A: Localisation errors for a single dipole source model averaged over 8 single accessory pathways, between 4 and 40 ms after the onset. Panel B: Localisation errors for a two-dipole source model averaged over 8 single accessory pathways, between 4 and 40 ms after the onset

Although the two-dipole model reflects well qualitative features of the propagated activation wavefront, it is less suitable for localising the single sites of early activation than the single-dipole model. Figure 4 comprehensively compares the accuracy of the localisation when using both models, with the evident superiority of the single-dipole model. The reason for the poorer performance of the two-dipole model is due to the fact that such a model – as explained above – localises both leading edges of the activation wavefront, which are progressively moving away from the actual site of preexcitation. On the other hand, single-dipole model reflects the centre of gravity of the activation. Depending on the noise level, localisation errors in Figure 4 reach minimum at different times after the

onset. In the case of the two-dipole model, the minimum is reached when both dipoles are far away from the actual onset (see Figure 3).

Figure 5 illustrates localisation results based on BSPMs and MFMs for the pair of RAL/RL accessory pathways (case 1a-1c). One can see that dipoles are clearly separated and located close to the actual locations of accessory pathways. In this specific case, the localisation errors attained a minimum at 20 ms after the onset of activation (11 ± 1 mm and 5 ± 1 mm for BSPMs and 9 ± 2 mm and 6 ± 1 mm for MFMs).

Figure 6 compares the accuracy of localisation when using different data types to localise dual accessory pathways in the presence of different noise levels. Table 2 summarises the localisation results for different typical measuring conditions. For typical RMS noise level of 5 μV and 120 fT, we found that two-dipole localisation reached minimum between 12 ms and 24 ms after the onset of activation. The average localisation errors were between 5 and 21 mm ($12 \pm 6/11 \pm 6$ mm at 20 ms for the first/second dipole, respectively) for the BSPMs and between 3 and 20 mm ($11 \pm 5/12 \pm 9$ mm at 24 ms) for the MFMs. Localisation errors were on average smaller for the pairs of accessory pathways located on the right side (cases 1a-1b, 1a-1c, 1a-1d) than for those located on the left side (cases 2a-2b, 2a-2c, 2a-2d); they were 8 mm versus 14 mm for the BSPMs and 7 mm versus 11 mm for the MFMs. RMS levels of simulated BSPMs were, at 20 ms after the onset of activation, between 104 μV (case 2a-2b) and 164 μV (case 1a-1c); RMS levels of simulated MFMs were at the same time instant between 0.9 pT (case 2a-2b) and 6.8 pT (case1a-1d).

When including magnetic leads near the anterior and posterior torso (in total 128 sites) to provide a lead arrangement equivalent to that of the potentials, the average localisation errors slightly improved and were in the presence of RMS noise of 120 fT between 2 and 14 mm ($10 \pm 5/8 \pm 6$ mm at 20 ms). Range of localisation errors degraded to 8–22 mm ($18 \pm 8/18 \pm 9$ mm at 28 ms) for BSPMs at 20 μV noise level, and to 3–26 mm ($14 \pm 8/15 \pm 11$ mm at 24 ms) for 64-lead and to 4–17 mm ($12 \pm 8/10 \pm 6$ mm at 24 ms) for 128-lead MFMs at 300 fT noise level.
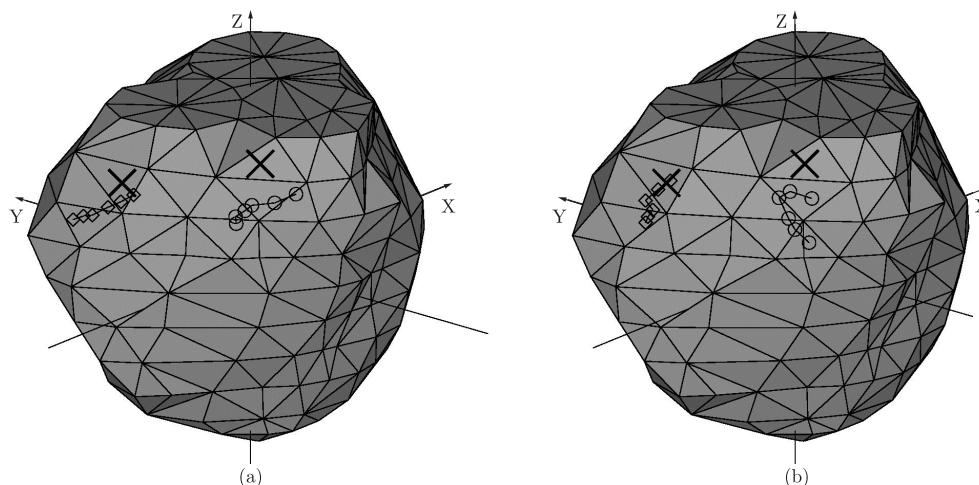

Fig. 5. Localisation results for a RAL/RL dual accessory pathways at different time instants (from 16 to 36 ms after the onset) when using (a) 117-BSPMs and (b) 64-MFMs
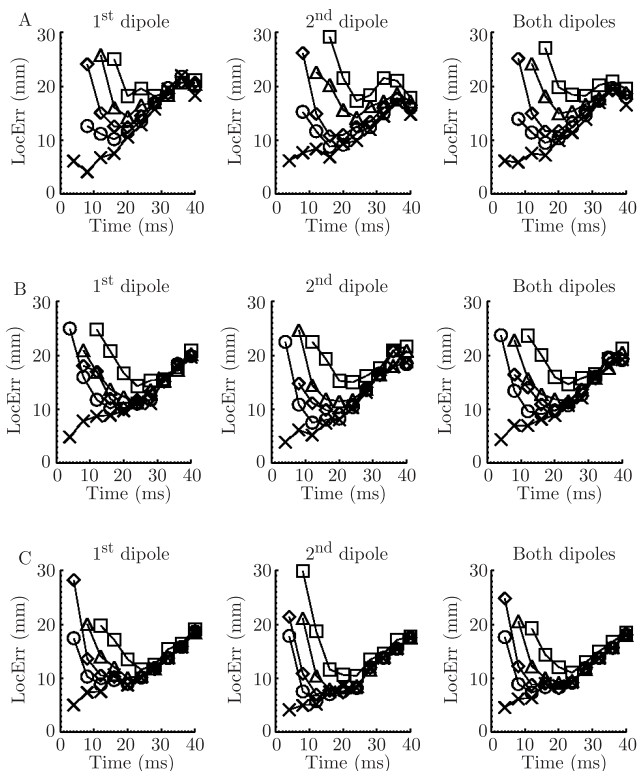
198

Fig. 6. Accuracy of localising dual accessory pathways obtained with a two dipole source model in the presence of different noise levels when using 117-lead body surface potentials (Panel A; "cross" – no noise, "circle" – RMS noise level of 2.5 µV, "diamond" – 5 µV, "triangle" – 10 µV, and "square" – 20 µV), and 64-lead and 128-lead magnetic field (Panels B and C; "cross" – no noise, "circle" – noise 30 fT, "diamond" – 60 fT, "triangle" – 120 fT, and "square" – 300 fT)

Localisation errors due to inaccuracies in rendering individualised torso boundaries reached their minimum between 16 and 28 ms after the onset. Modelling errors, defined as differences between leads on the individualised torso and corresponding leads on the "standardised" torso, were up to 32 mm with mean value 14 ± 7 mm. The localisation errors were on average in the range of 11 to 39 mm ($24 \pm 18/30 \pm 13$ mm at 20 ms) for the BSPMs and of 12 to 36 mm ($20 \pm 13/29 \pm 14$ mm at 20 ms) for the MFMs. Visual inspection of inversely

calculated dipole positions revealed that they were often distal to the actual locations of accessory pathways and sometimes fell out of anatomically plausible region.

2.3. Discussion. Results of this study demonstrate that a source model consisting of two dipoles embedded in the torso volume conductor model could be useful in localising dual accessory pathways providing that

(i) we know the torso geometry of a given patient and that
(ii) we have *a priori* knowledge of the presence of dual accessory pathways.

Both aspects need to be determined noninvasively to be of a clinical use.

The first requirement could be fulfilled using various computer-aided tomographic methodologies for noninvasively rendering anatomical geometry [15,16]. The second, more stringent requirement could be fulfilled by applying electrocardiographic imaging (ECGI), i.e., by mathematically calculating epicardial potentials from torso potentials [17,18]. Our recent study [19] and studies of others [20,21] indicated that ECGI could greatly enhance resolving power of potentials measured on the torso surface. Moreover, the epicardial potentials provide morphological features (such as multiple minima) that clearly point towards the presence of multiple ventricular events. The two-dipole inverse solution could thus be useful – whenever electrocardiographic imaging indicates so – in providing adjuvant methodology for localising dual accessory pathways.

In simulations, we used an assumption of a homogeneous torso model that clearly differs from the actual measurement conditions. On the other hand, very recent study of Ramanathan and Rudy [22,23] indicated that inhomogeneities primarily affect the potential magnitudes and not the potential patterns. Whether interindividual variability in position and size of inhomogeneities/anisotropies in the torso affects only the magnitude of inversely-calculated dipoles and not their position remains to be determined. We simulated "pure" preexcitation sequences without interference from the atrial repolarisation, which may affect the localisation of equivalent dipoles

Table 2
Localisation results for different measuring conditions: a) typical RMS noise levels,
b) increased RMS noise levels, and c) in the presence of modelling errors

	Data type	RMS noise	Error range	Average error $\pm SD$ First / second dipole	Optimal time
a)	117 BSPM	5µV	5 to 21 mm	$12 \pm 6/11 \pm 6$ mm	20 ms
	64 MFM	120 fT	3 to 20 mm	$11 \pm 5/12 \pm 9$ mm	24 ms
	128 MFM	120 fT	2 to 14 mm	$10 \pm 5/8 \pm 6$ mm	20 ms
b)	117 BSPM	20 µV	8 to 22 m	$18 \pm 8/18 \pm 9$ mm	28 ms
	64 MFM	300 fT	3 to 26 mm	$14 \pm 8/15 \pm 11$ mm	24 ms
	128 MFM	300 fT	4 to 17 mm	$12 \pm 8/10 \pm 6$ mm	24 ms
c)	Modelling errors: inaccuracies in rendering individualised torso boundaries				
	117 BSPM	5 µV	11 to 39 mm	$24 \pm 18/30 \pm 13$ mm	20 ms
	64 MFM	120 fT	12 to 36 mm	$20 \pm 13/29 \pm 14$ mm	20 ms

V. Jazbinsek, R. Hren, and Z. Trontelj

within the first 16 ms after the onset of preexcitation. In clinical applications, such conditions could be potentially achieved by a proper subtraction of the atrial repolarisation from the signal. Results of our study also suggest that the magnetocardiographic inverse solution is at least as accurate as the electrocardiographic inverse solution when using a two-dipole model.

Overall, our results suggest that the two-dipole inverse solution could provide an adjuvant tool for localising dual fibres in patients with preexcitation syndromes. However, it also appears that our model cannot be used for characterising ventricular events, that is, for distinguishing between single and multiple events. Only when the presence of dual concurrent events is established, the two-dipole model could be used for aiding localisation of each of the two accessory pathways.

3. Randomly displaced BSPM leads

3.1. Methods. To simulate displacement of leads on the torso surface, we generated a database of 7 torso models. We modified these nodes that corresponded to positions of 117 leads on a surface of the realistic male torso model (Fig. 7a). For each lead position on the torso surface, we defined a local tangential plane and then displaced the lead along two mutually perpendicular directions on that plane. Random displacements were generated by uniform distribution on the interval $D \cdot \sqrt{6} \cdot [-0.5, 0.5]$, where D was a root-mean-square (RMS) value of a displacement on the tangential plane. We assigned D equal to 10 mm in all cases. Average ($\pm SD$) three-dimensional distance between displaced and reference leads

was 9.4 ± 3.4 mm. Figure 7b shows locations of the displaced leads in one of the torso models. Using simulated maps as the input data, we performed localisation ("inverse solution") for a single dipole source in the realistic male torso model with standardised placement of leads following a Levenberg-Marquardt least-squares fitting algorithm [5,9]. The initial estimate of the single dipole location was at the geometrical centre of the heart. As a measure for accuracy of the localisation we used the localisation error, defined as the distance between the location of the best-fitting single dipole and the site of preexcitation in the ventricular model.

We initiated activation sequences at a total of 8 single preexcitation sites located along RL (1a, 1b, 1c, 1d) and LL (2a, 2b, 2c, 2d) aspects of the AV ring of the epicardium (Fig. 1). For each activation sequence and each torso model with randomly displaced leads, we simulated body surface potentials (at 117 sites) at 4-ms increments within the first 40 ms after the onset of preexcitation. To simulate measuring conditions, we calculated for each of 8 preexcitation sites, each time instant, and each torso model, body surface potentials with added random Gaussian noise at four different RMS levels: 5, 10, 20, and 50 µV. We generated 10 different noise distributions for each noise level. The inverse procedure was performed at 4-ms intervals for each of the 8 preexcitation sites using torso model with the standardised placement of leads.

3.2. Results. Figure 8a shows the average localisation errors and their standard deviations calculated at each time instant from 4 individual errors for RL and LL preexcitation sites with

(a) Standardised leads   (b) Displaced leads
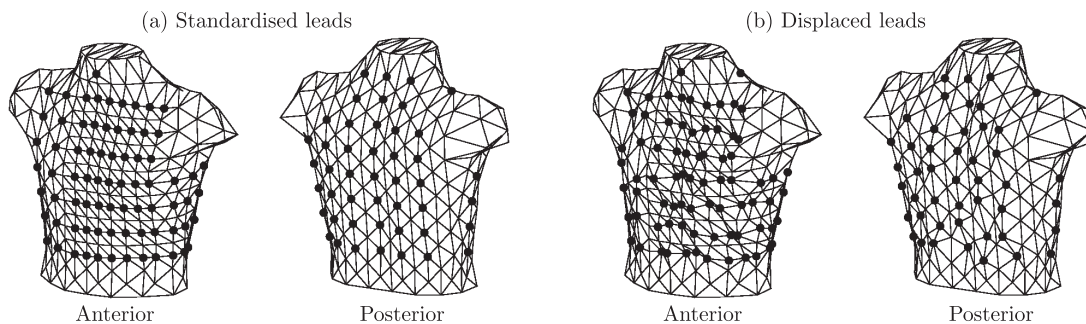
Anterior   Posterior   Anterior   Posterior

Fig. 7. The anterior and posterior views of the realistic male torso model: a) with the 117 standardised lead positions and b) with randomly displaced leads
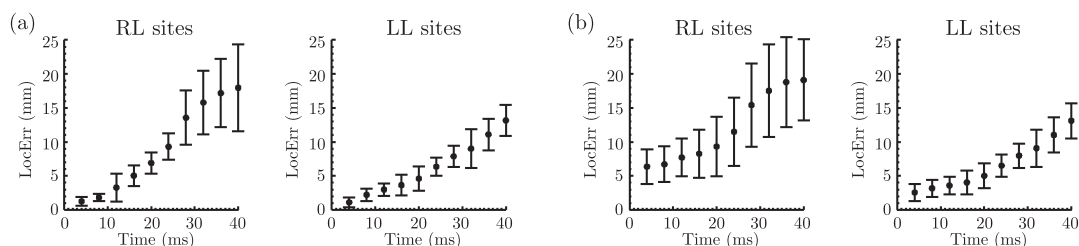

Fig. 8. Average localisation errors (in mm) shown as a function of time after the onset of preexcitation for RL and LL sites for: a) the torso model with standardised placement of leads was used for both the forward and inverse solutions and b) seven torso models with displaced leads were used for the forward solution and the torso model with standardised placement of leads was used for the inverse solution. No measurement noise was added. Error bars indicate $\pm$ standard deviation

no displaced leads and no noise present. For both RL and LL sites, the localisation errors gradually increased through the preexcitation sequence (e.g., for RL sites, 3.3 ± 2.0 mm at 8 ms and 13.6 ± 4.0 mm at 28 ms after the onset) which is in agreement with the widespread notion that the single dipole can accurately represent the true cardiac sources only when the bioelectric activity of the heart is confined to small regions (diameter $\approx$ several mm). The average localisation errors remained below 10 mm within the first 24 ms after the onset of preexcitation.
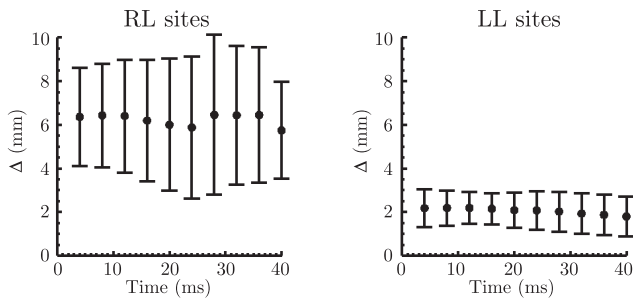

Fig. 9. Average difference ($\triangle$) for RL and LL preexcitation sites between localisation obtained from simulations using torso models with displaced leads and corresponding localisation calculated from simulations using the torso model with standardised placement of leads (reference)

Figure 8b shows the localisation errors for RL and LL sites when torso models with displaced leads were used for the forward solution and the torso model with standardised placement of leads was used for the inverse solution. The localisation errors for RL preexcitation sites were markedly larger than in the absence of displaced leads during the early phase of preexcitation (e.g., at 20 ms after the onset of preexcitation, 9 ± 4 mm versus 7 ± 1 mm). Later in the sequence, localisation results suggest that the inaccuracies due to the size and shape of the activation wavefront dominate the localisation accuracy. It appears that displacement of leads did not affect accuracy of localisation for LL sites (see below).

Figure 9 illustrates the localisation errors due to lead displacements alone. This figure was constructed by comparing localisation obtained from simulations using the torso models with displaced leads to corresponding localisation calculated from simulations using the torso model with standardised placement of leads. As can be expected, the localisation error remained relatively constant throughout the preexcitation sequence (e.g., for RL sites, 6.4 ± 2.6 mm at 12 ms and 6.5 ± 3.7 mm at 28 ms after the onset). However, the separate impact of the lead displacement on the localisation accuracy was significantly more pronounced for RL sites than for LL sites (e.g., at 20 ms after the onset, 6.0 ± 3.0 mm versus 2.1 ± 0.8 mm).

This observation is in agreement with forward simulations exploring pattern differences of BSPMs due to the displacement of leads. Using BSPMs calculated by the standardised placement of leads as the reference, we obtained significant differences in correlation coefficients between RL and LL sites (average correlation of 0.980 ± 0.012 versus 0.9971 ± 0.0004).

Figures 10 a, b show average and maximum localisation errors calculated at each time instant for RL and LL preexcitation sites in the presence of four different levels of noise. Depending on the noise level, localisation errors reached the minimum between 12 and 24 ms after the onset for RL sites, and between 16 and 32 ms after the onset for LL sites. For RL sites, maximum errors were 21, 22, 25, and 39 mm at 20 ms after the onset for RMS noise levels of 5, 10, 20, and 50 µV, respectively. For LL sites, maximum errors were 14, 17, 23, and 75 mm at 20 ms after the onset for RMS noise levels of 5, 10, 20, and 50 µV, respectively.

Our results suggest that the effect of measurement noise on localisation depended on a signal to noise (S/N) ratio defined as a ratio between RMS values of BSPMs and a given noise level. In fact, the measurement noise markedly influenced both forward and inverse solutions when S/N was less than 5.

3.3. Discussion. In this study, we investigated the effects of inaccuracies in determining the lead positions and measurement noise on the inverse solution of single accessory pathways when using the single dipole source model. The findings of our study demonstrate that in the presence of measurement noise and lead displacement, average localisation errors were < 10 mm. At noise levels found during a typical BSPM recordings < 5 µV, optimal time interval for localisation was between 12 and 20 ms after the onset of preexcitation.
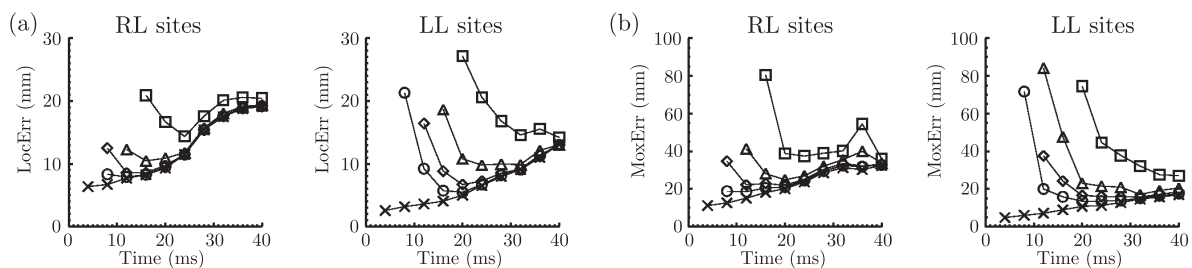

Fig. 10. Average localisation errors (in mm) shown as a function of time after the onset of preexcitation for RL and LL sites for four different RMS noise levels. Seven torso models with displaced leads were used for the forward solution and the torso model with standardised placement of leads was used for the inverse solution: "cross" – no noise, "circle" – RMS noise level of 5 µV, "diamond" – 10 µV, "triangle" – 20 µV, and "square" – 50 µV

Our study has some limitations (see also Section 2.3 above). Firstly, we used anatomically detailed, but still idealised model of the human ventricular myocardium. Secondly, we used homogeneous torso model. Thirdly, we simulated pure preexcitation sequences without interference from atrial repolarisation or fusion with normal ventricular activation. Finally, our results were obtained for a specific 117-lead BSPM configuration.

Overall, our study indicated that it is important to localise the preexcitation activity very early in the sequence (< 20 ms after the onset). Within this time interval, the bioelectric activity of the ventricles is confined to a single very small volume and the single dipole can accurately point to the preexcitation. In clinical applications, localisation will depend on proper subtraction of the atrial repolarisation from the electrocardiographic signals. aaa

4. Selection of optimal leads

4.1. Methods. To reduce the number of recording sites, we followed the statistical estimation technique [6], where the magnetic field or electric potential at unmeasured sites x^e are estimated from their values at measured sites x^m by a linear transformation T such that

$$x^e = Tx^m = K_{um}K_{mm}^{-1}x^m, \tag{3}$$

where K_{mm} is a covariance matrix of the measured potential/field and K_{um} is a cross covariance matrix between the measured and unmeasured potential/field. This estimator minimises the root mean square error (RMS). An optimal subset of recording sites was found by sequential algorithm [6]; the recording site that had the highest correlated power ("information content") with all other sites was selected at each step.

To evaluate the above algorithm, we used database consisted of BSPMs and MFMs obtained from 4 subjects with no known cardiac diseases. A protocol is explained in details elsewhere [24]. Briefly, MFMs over a large area with diameter of 37 cm near the front and the back thorax were obtained with a dense 119 B_z channels on each side (Fig. 11a) with a sampling rate of 1 kHz. In addition, 148 lead BSPMs were recorded (Fig. 11b). We used various combinations of these data sets as learning (x^m) and test (y^m) sets. The noise level estimated from measured data in the region before P onset, were 200 fT and 10 μV for the MFMs and BSPMs, respectively.

We evaluated the quality of estimated quantities y^e from

Eq. (3) by comparing them with the measured values y^m. We used various criteria, like RMS error and maximum (MAX) error, relative difference (RD) and correlation coefficient (CC), which are for the map at time t_j and N_u unmeasured sites defined as

$$\begin{aligned} \mathrm{RMS}(t_j) &= \sqrt{\sum\nolimits_{i=1}^{N_u} \left(y_{i,j}^e - y_{i,j}^m\right)^2 / N_u}, \\ \mathrm{MAX}(t_j) &= \max|y_{i,j}^e - y_{i,j}^m|_{i=1}^{N_u}, \\ \mathrm{RD}(t_j) &= 100\sqrt{\sum\nolimits_{i=1}^{N_u} \left(y_{i,j}^e - y_{i,j}^m\right)^2 / \sum\nolimits_{i=1}^{N_u} \left(y_{i,j}^m\right)^2}, \\ \mathrm{CC}(t_j) &= \sum\nolimits_{i=1}^{N_u} y_{i,j}^e y_{i,j}^m / \sqrt{\sum\nolimits_{i=1}^{N_u} \left(y_{i,j}^e\right)^2 \left(y_{i,j}^m\right)^2}. \end{aligned} \tag{4}$$

To evaluate the similarity between the estimated and measured data set in different time intervals, like P-wave, QRS, S-ST, ST-T and PQRST, we calculated the mean values and standard deviations of the RMS, MAX, RD and CC values. In addition, we calculated the amplitude-weighted correlation coefficient (WCC) and the isointegral maps on those time intervals. The WCC on the time interval from t_1 to t_2 is defined as [25],

$$\begin{aligned} \mathrm{WCC} &= \sqrt{\sum\nolimits_{t_j=t_1}^{t_2} \mathrm{W}(t_j)\mathrm{CC}(t_j)}, \\ \mathrm{W}(t_j) &= \sum\nolimits_{i=1}^{N_u} \left(y_{i,j}^m\right)^2 / \sum\nolimits_{t_j=t_1}^{t_2} \sum\nolimits_{i=1}^{N_u} \left(y_{i,j}^m\right)^2. \end{aligned} \tag{5}$$

We defined the integral maps as an average over all maps on the selected time interval.

To evaluate the influence of limited lead selection on localisation accuracy, we used all simulated maps obtained for single preexcitation sites (Fig. 1) as a learning database. Then we selected optimal subsets with 8, 10, 12, ... 32 leads for the 64 and 128 lead MFM, and 117 lead BSPM. For comparison, we have generated also random subsets of 8,10,12, ... 32 leads. Then we localised single preexcitation sites with a single dipole model using optimally and randomly obtained subsets. Finally, we compared these localisation results with those obtained by the complete 64 and 128 lead MFM, and 117 lead BSPM.

4.2. Results. Figure 11 shows the distribution of the first 30 selected recording sites for a case where a combination of data sets measured on three volunteers are used as a learning data set x^m. The whole PQRST interval was used for x^m, which included 500–700 map frames per volunteer. For the BSPM
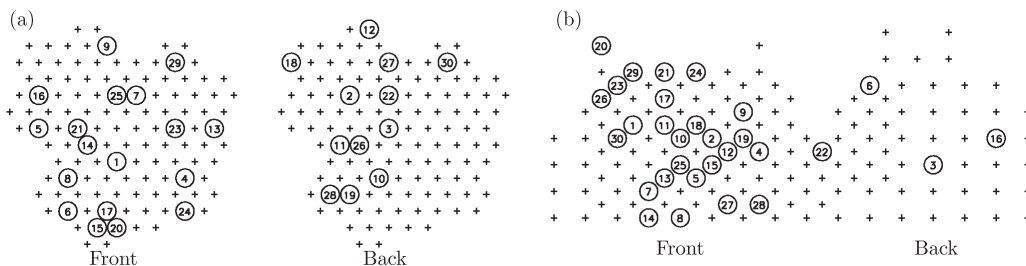

Fig. 11. Example of optimally selected recording sites when using measured data of three volunteers as a training set: a) 238 anterior/posterior MFM and b) 148-lead BSPM. Encircled numbers show the order of selected sites
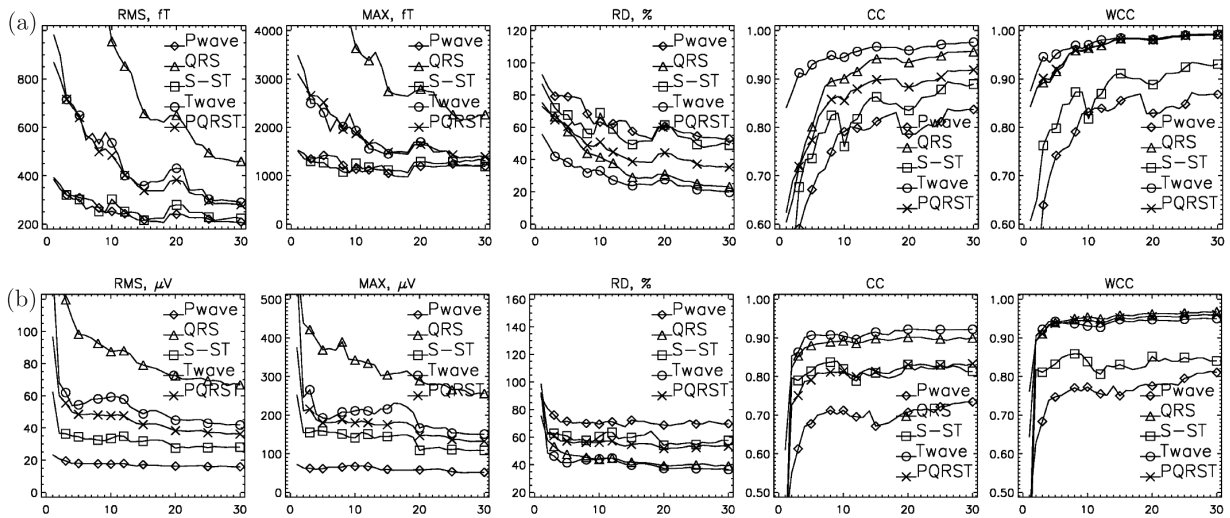
Fig. 12. Mean RMS, MAX, RD, CC and WCC vs. number of selected sites for a) MFMs and b) BSPMs when using all four combinations of learning (x^m) and test (y^m) data sets in cases where measurements on three of the four volunteers are used as x^m and measurements on the remaining volunteer are used as y^m. After each selected site, maps (y^e) for the y^m are estimated from Eq. (1) and for each y^e, values of RMS, MAX, RD and CC are calculated from Eqs. (2–5). These results are then averaged over all maps on different time intervals, Pwave ("diamond"), QRS ("triangle"), S-ST ("square"), Twave ("circle") and PQRST ("cross"), and WCC is calculated from Eq. (5). Pwave interval is from the onset to the end of P, S-ST is a first 3/8 portion of the ST segment and Twave is from the end of S-ST to the end of T
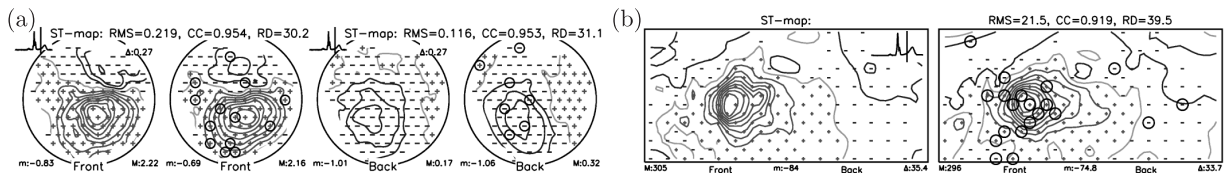

Fig. 13. Example of a) MFM and b) BSPM at the end of the S-ST interval after 20 selected channels from Figure 11. Here m and M are the minimal and the maximal map values and ∇ is a step between the two isolines. All these values are in pT for the MFM and in μV for the BSPM. Positions of measured sites are shown by $+$ and $-$ in accordance with the sign of data. Estimated maps are displayed right to the corresponding measured maps. The selected sites are encircled, and RMS, CC and RD values are displayed above the estimated maps
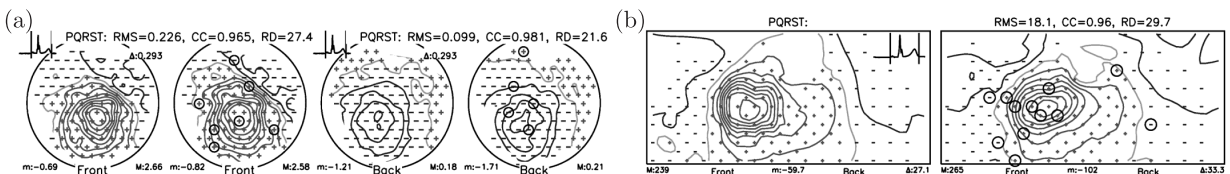

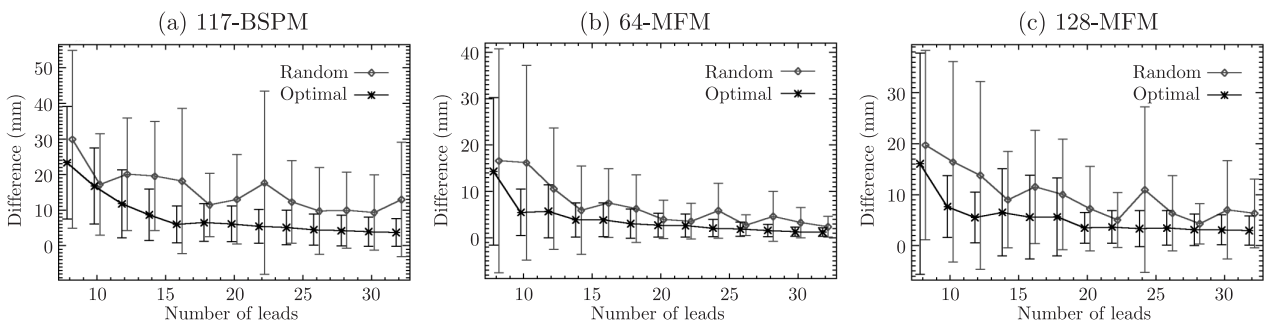Fig. 14. PQRST – Integral maps after 12 optimally selected channels

Fig. 15. Average difference between localisation results obtained by the complete lead systems versus optimally ("cross") and randomly ("diamond") selected subset of leads: a) 117 lead BSPM, b) 64 lead MFM and c) 128 lead MFM. Error bars indicate $\pm$ standard deviation

most of sites were positioned on the anterior side of the thorax, while in the case of the MFM optimal recording sites were more evenly distributed over front and back.

Figure 12 shows average RMS, MAX, RD, CC and WCC when the data sets measured on three volunteers are used as x^m and the data measured on the remaining volunteer is used as y^m. Results show that most of the information is stored in the first 10 to 20 optimally chosen sites. There is little information gain by selecting more than 20 sites. Average RMS, MAX, RD, CC and WCC calculated from the maps with 20 selected sites, obtained at different time intervals, are in the range of 240–650 fT, 1200–2800 fT, 28–60%, 0.79–0.97 and 0.83–0.98 for the MFMs, and 16–72 µV, 60–290 µV, 37–80%, 0.71–0.92 and 0.78–0.96 for the BSPMs, respectively. The RMS and MAX errors are higher for the QRS time interval, which may be expected since those errors are related to the amplitude of the signal. Average CCs and WCCs, which reflect similarity of the signal shape, are worse for the S-ST and especially for the P wave intervals, where the signal to noise ratio is lower. The WCCs are higher because the effect of noise is reduced during periods when the signal is small. Average RDs, which are sensitive both to the amplitude and the shape, are better for the QRS and the T wave regions.

Figure 13 shows an example of measured and estimated MFM and BSPM when 20 sites are selected. Values of RMS, CC and RD are 219 fT, 0.954 and 30% for the anterior MFM, 116 fT, 0.953 and 31% for the posterior MFM, and 21.5 µV, 0.919 and 40% for the BSPM, respectively.

When comparing integral maps calculated from measured and estimated data sets, we found out that average values of RMS, CC and RD for integral maps estimated from 12 selected sites are in the range of 190–580 fT, 18–58% and 0.83–0.98 for MFMs, and 14–65 µV, 35–80% and 0.58–0.94 for BSPMs, respectively. These ranges are comparable with those obtained for single maps estimated from 20 sites (see, Fig. 12, and description in the text). That may be expected since the procedure of averaging tends to reduce the information content.

Figure 14 shows an example of measured and estimated PQRST integral MFMs and BSPMs when 12 sites are selected. Values of RMS, CC and RD are 226 fT, 0.965 and 24% for the anterior MFM, 99 fT, 0.981 and 22% for the posterior MFM, and 18.1 µV, 0.96 and 30% for the BSPM, respectively.

Figure 15 compares the localisation accuracy when using both random and optimal limited selection of leads. There is evident superiority of the optimal selection for all measuring modalities (117 lead BSPM, 64 and 128 lead MFM). After 20 optimally selected leads, we obtain dipole locations, which are on average only within few millimetres away from the locations calculated from complete lead systems. It seems that 20 optimally selected leads may be sufficient for localisation of single preexcitation sites with the single-dipole model.

4.3. Discussion. This study is the first attempt to examine redundancy and uniqueness of MFM signal information. The main finding of our study is that markedly smaller number of leads, in comparison to that currently employed in systems for both BSPM and MFM recordings, may be sufficient to extract clinically pertinent information. We obtain the average WCC of 0.98 ± 0.01 for estimated MFMs from 20 sites in the whole PQRST interval. This is evidently better then results in [25] (0.94 ± 0.02 and 0.93 ± 0.03), where the conversion between two MFM measuring system was evaluated by two methods, multipole expansion and minimum norm estimates.

Our results corroborate the finding in [6] that the "optimal" lead selection is non-unique, i.e., that slightly different position of the first lead could generate quite different lead sets, which perform equally well. The database, used to evaluate the selection procedure in our study, consisted of healthy volunteers. The natural extension of this database could include patients with old myocardial infarction. The methodology developed in this study could also be used in selecting the optimal lead configuration for specific type of cardiac abnormalities, e.g., the limited array of magnetocardiographic leads for monitoring ST-segment changes caused by acute coronary ischemia.

REFERENCES

[1] I. Singer, *Interventional Electrophysiology*, Baltimore: Williams and Wilkins, 1997.

[2] P. Savard, A. Ackaoui; R.M. Gulrajani, R. Nadeau, F.A. Roberge; R. Guardo, and B. Dube, "Localization of cardiac ectopic activity in man by a single moving dipole. Comparison of different computation techniques", *J. Electrocardiol.* 18, 211–222 (1985).

[3] J. Nenonen, C.J. Purcell, B.M. Horáček, G. Stroink, and T. Katila, "Magnetocardiographic functional localization using a current dipole in a realistic torso", *IEEE Trans. Biomed. Eng.* 38, 658–664 (1991).

[4] V. Jazbinsek, R. Hren, G. Stroink, B.M. Horáček, and Z. Trontelj, "Value and limitations of an inverse solution for two equivalent dipoles in localizing dual accessory pathways", *Med. Biol. Eng. Comput.* 41, 133–140 (2003).

[5] V. Jazbinsek and R. Hren, "Influence of randomly displaced BSPM leads on the identification of ventricular preexcitation sites", *Biomed. Eng.* 44 (Suppl. 2), 104–107 (1999).

[6] R.L. Lux, C.R. Smith, R.F. Wyatt, and J.A. Abildskov, "Limited lead selection for estimation of body surface potential maps in electrocardiography", *IEEE Trans. Biomed. Eng.* 25, 270–276 (1978).

[7] J.A. Abildskov and L.S. Green, "The recognition of arrhythmia vulnerability by body surface electrocardiographic mapping", *Circulation* 75 (Suppl III), 79–83 (1987).

[8] R.L. Lux, "Electrocardiographic mapping: Noninvasive electrophysiological cardiac imaging. *Circulation* 87, 1040–1042 (1993).

[9] R. Hren, G. Stroink, and B.M. Horáček, "Accuracy of single-dipole inverse solution when localising ventricular preexcitation sites: simulation study", *Med. Biol. Eng. Comp.* 36, 323–329 (1998).

[10] R. Hren, G. Stroink, and B.M. Horáček, "Spatial resolution of body surface potential maps and magnetic field maps: A simulation study applied to the identification of ventricular preexcitation sites", *Med. Biol. Eng. Comp.* 36, 145–157 (1998).

[11] R. Hren, "Value of epicardial potential maps in localizing pre-excitation sites for radiofrequency ablation: A simulation study", *Phys. Med. Biol.* 43, 1449–1468 (1998).

[12] C. Purcell and G. Stroink, "Moving dipole inverse solutions using realistic torso models", *IEEE Trans. Biomed. Eng.* 38, 82–84 (1991).

[13] E. Macchi, G. Arisi, and B. Taccardi, "Identification of ectopic ventricular foci by means of intracavitary potential mapping: a proposed method", *Acta Cardiol.* 47, 421–33 (1992).

[14] B. Taccardi, E. Macchi, R.L. Lux, P.R. Ershler, S. Spaggiari, S. Baruffi, and Y. Vyhmeister, "Effect of myocardial fiber direction on epicardial potentials", *Circulation* 90, 3076–3090 (1994).

[15] J. Lotjonen, I.E. Magnin, J. Nenonen, and T. Katila, "Reconstruction of 3-D geometry using 2-D profiles and a geometric prior model", *IEEE Trans. Med. Imaging* 18, 992–1002 (1999).

[16] D. van't Ent, J.C. de Munck, and A.L. Kaas, "A fast method to derive realistic BEM models for E/MEG source reconstruction", *IEEE Trans. Biomed. Eng.* 48.,1434–1443 (2001).

[17] B.M. Horáček, R.G. de Boer, L.J. Leon, and T.J. Montague, "Human epicardial potential distributions computed from body surface available data", in *Advances in Body Surface Potential Mapping*, pp. 47–54, Nagoya, University of Nagoya Press, 1983.

[18] B.M. Horáček and J.C. Clements, "The inverse problem of electrocardiography: A solution in terms of single- and double-layer sources on the epicardial surface", *Math. Biosci.* 144, 119–145 (1997).

[19] R. Hren and G. Stroink, "Noninvasive characterisation of multiple ventricular events using electrocardiographic imaging", *Med. Biol. Eng. Comp.* 39, 447–454 (2001).

[20] H.S. Oster, B. Taccardi, R.L. Lux, P.R. Ershler, and Y. Rudy, "Noninvasive electrocardioghraphic imaging: reconstruction of epicardial potentials, electrograms, and isochrones and localization of single and multiple electrocardiac events", *Circulation* 96, 1012–1024 (1997).

[21] C.J. Penney, J.C. Clements, and B.M. Horáček, "Non-invasive imaging of epicardial electrograms during controlled myocardial ischemia", in *Computers in Cardiology*, pp. 103–106, Los Alamitos, IEEE Computer Society Press (2000).

[22] C. Ramanathan and Y. Rudy, "Electrocardiographic imaging: I. Effect of torso inhomogeneities on body surface electrocardiographic potentials", *J. Cardiovasc. Electrophysiol.* 12, 229–240 (2001).

[23] C. Ramanathan and Y. Rudy, "Electrocardiographic imaging: I. Effect of torso inhomogeneities on noninvasive reconstruction of epicardial potentials, electrograms, and isochrones", *J. Cardiovasc. Electrophysiol.* 12, 241–252, 2001.

[24] V. Jazbinsek, O. Kosch, P. Meindl, U. Steinhoff, Z. Trontelj, and L. Trahms, "Multichannel vector MFM and BSPM of chest and back", in *12th Int. Conf. on Biomagnetism*, pp. 583–586, Espoo, Helsinki Univ. of Technology, (2001).

[25] M. Burghoff, J. Nenonen, L. Trahms, and T. Katila, "Conversion of magnetocardiographic recordings between two different multichannel SQUID devices", *IEEE Trans. Biomed. Eng.* 47, 869–875 (2000).